

Improving Efficiency of a High Work Turbine Using Nonaxisymmetric Endwalls—Part II: Time-Resolved Flow Physics

P. Schüpbach¹

e-mail: schuepbach@lec.mavt.ethz.ch

R. S. Abhari

Department of Mechanical and Process Engineering,
LEC, Laboratory of Energy Conversion,
ETH Zurich,
8092 Zurich, Switzerland

M. G. Rose

Institute of Aeronautical Propulsion,
University of Stuttgart,
70569 Stuttgart, Germany

T. Germain

I. Raab

J. Gier

MTU Aero Engines GmbH,
Dachauer Strasse 665,
80995 München, Germany

This paper is the second part of a two part paper that reports on the improvement of efficiency of a one and a half stage high work axial flow turbine. The first part covered the design of the endwall profiling, as well as a comparison with steady probe data; this part covers the analysis of the time-resolved flow physics. The focus is on the time-resolved flow physics that leads to a total-to-total stage efficiency improvement of $1.0\% \pm 0.4\%$. The investigated geometry is a model of a high work ($\Delta h/U^2 = 2.36$), axial shroudless HP turbine. The time-resolved measurements have been acquired upstream and downstream of the rotor using a fast response aerodynamic probe (FRAP). This paper contains a detailed analysis of the secondary flow field that is changed between the axisymmetric and the nonaxisymmetric endwall profiling cases. The flowfield at the exit of the first stator is improved considerably due to the nonaxisymmetric endwall profiling and results in reduced secondary flow and a reduction in loss at both hub and tip, as well as a reduced trailing shed vorticity. The rotor has reduced losses and a reduction in secondary flows mainly at the hub. At the rotor exit, the flow field with nonaxisymmetric endwalls is more homogenous due to the reduction in secondary flows in the two rows upstream of the measurement plane. This confirms that nonaxisymmetric endwall profiling is an effective tool for reducing secondary losses in axial turbines. Using a frozen flow assumption, the time-resolved data are used to estimate the axial velocity gradients, which are then used to evaluate the streamwise vorticity and dissipation. The nonaxisymmetric endwall profiling of the first nozzle guide vane show reductions in dissipation and streamwise vorticity due to the reduced trailing shed vorticity. This smaller vorticity explains the reduction in loss at midspan, which is shown in the first part of the two part paper. This leads to the conclusion that nonaxisymmetric endwall profiling also has the potential of reducing trailing shed vorticity. [DOI: 10.1115/1.3103926]

1 Introduction

In order to improve efficiency and reduce costs, turbine designers strive to reduce the number of stages and blades per row. Therefore, both stage loading and lift coefficients are being continuously pushed up. With increasing stage loading, the secondary loss rises and can be up to half of the total loss generated [1]. In low aspect ratio turbines such as that investigated here (NGV1: 0.87, Rotor: 1.17, and NGV2: 0.82), the losses are even more pronounced as the hub and tip secondary flows interact closely with each other. A detailed review of secondary flows in cascades can be found in Refs. [2,3]. The losses are generated in part from dissipation of the kinetic energy of rotation of the vortices, little of which is recovered in the following blade rows. Schlienger et al. [4] gave a detailed analysis of secondary flows in a shrouded axial turbine (Fig. 1).

In the past a variety of methods have been developed to reduce secondary flows. One approach is the active methods such as boundary layer blowing investigated by Sturm et al. [5] and Biesinger [6], which showed reductions in loss.

However, many studies of passive methods have also been reported. The most frequently used are blade leaning, and axisymmetric and nonaxisymmetric endwall profiling. Harrison [7] inves-

tigated in detail the effect of blade leaning. He reported that there is no loss reduction within the row in which blade leaning is applied. The performance increase comes rather from an improved flowfield into the subsequent blade rows.

The concept of axisymmetric endwall profiling was introduced by Dejc et al. [8] as a contraction of the annulus from the leading edge to the trailing edge. A loss reduction of up to 20 % was verified in linear cascade tests by Morris et al. [9]. The most promising endwall geometry incorporated a strong contraction early in the passage (often known as the “Russian kink”) that results in a thinner boundary layer. Atkins [10] investigated different endwall contours in a linear cascade. He showed that the losses near the endwall can be influenced by its shape and the resulting pressure field. Sauer et al. [11] described a loss reduction by leading edge modifications.

During the past decade, emerging computational fluid dynamics (CFD) capabilities have made it possible to design more complex three-dimensional nonaxisymmetric endwalls. Nonaxisymmetric profiling using such capabilities was first introduced by Rose [12]. His goal was to have a more homogenous pressure field at the exit platform, which would reduce the turbine disk coolant massflow. Later Hartland [13] and Ingram [14] investigated nonaxisymmetric endwall profiling in the Durham linear cascade and showed that secondary loss reductions of 24% could be attained. Brennan [15] et al. and Rose et al. [16] demonstrated an increase in stage efficiency of 0.4% from computations and $0.59\% \pm 0.25\%$ from measurements. Duden et al. [17] and Eymann et al. [18] investigated the combined effects of endwall contouring and blade thickening.

¹Corresponding author.

Contributed by the International Gas Turbine Institute of ASME for publication in the JOURNAL OF TURBOMACHINERY. Manuscript received July 9, 2008; final manuscript received January 27, 2009; published online January 12, 2010. Review conducted by David Wisler. Paper presented at the ASME Turbo Expo 2008: Land, Sea and Air (GT2008), Berlin, Germany, June 9–13, 2008.

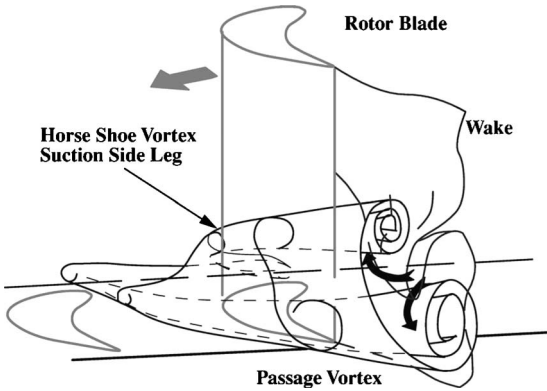


Fig. 1 Secondary flow model by Schlienger [4]

The work presented here improves our understanding of the time-resolved flow physics that lead to an improved stage efficiency. Furthermore, the work shows the potential of reducing both the endwall secondary losses and the losses at midheight in low aspect ratio turbines by reducing the trailing shed vorticity.

2 Experimental Method

The experimental investigation was performed in the research turbine “LISA” in the Laboratory of Energy Conversion at the Swiss Federal Institute of Technology. Recently the existing two-stage, shrouded turbine configuration [19] was redesigned as a one and a half unshrouded turbine that it is representative of a high work, cooled turbine. Further details of the new design are presented by Behr et al. [20] but its salient features are described below.

2.1 Experimental Turbine Facility. The air loop of the facility is quasiclosed and includes a radial compressor, a two-stage water to air heat exchanger, and a calibrated venturi nozzle for mass flow measurements. Upstream of the turbine section is a 3 m flow conditioning stretch to ensure a homogenous flowfield. Additionally the flow undergoes an acceleration ahead of the turbine section in order to reduce the significance of remaining flow uniformities from upstream. At the exit of the turbine section, the air loop opens to atmosphere. A dc generator absorbs the turbine power and controls the rotational speed with an indicated accuracy of $\pm 0.02\%$ (± 0.5 rpm). A heat exchanger controls the inlet total temperature $T_{t,in}$ to an accuracy of $\pm 0.3\%$. A torque meter measures the torque on the rotor shaft. With the compressor ratio limited to $\Pi_{c,max}=1.5$, it is necessary to add a tandem deswirl vane arrangement to recover the static pressure at the exit of the second stator back to the ambient level, in order to reach the intended turbine pressure ratio of $\Pi_{1,5}=1.65$. The turbine is unshrouded with a nominal tip gap of 1% of the span. The variation in the tip gap between builds is less than 1% of the tip gap, which ensures good repeatability. At the exit of the first nozzle guide vane row, the flow is compressible with an exit Mach number of 0.53.

2.2 Measurement Technology. The unsteady flow field is measured with a fast response aerodynamic probe (FRAP), which was developed at the LEC [21,22]. The probe is capable of capturing unsteady flow features up to frequencies of 48 kHz based on measurements including the total and static pressures, flow yaw and pitch angles, and Mach number. The frequency bandwidth of the temperature is limited to a frequency of 10 Hz. However, the influence of the measured temperature on the velocity is very modest. The FRAP probe has a 1.8 mm tip diameter and is equipped with two sensors. The probe is operated in a virtual-four-sensor mode to measure three-dimensional, time-resolved flow properties. The data are acquired at a sampling rate of 200

Table 1 Uncertainty bandwidth of FRAP probe

| Yaw angle | Pitch angle | $p_t/(p_t-p_s)$ | $p_s/(p_t-p_s)$ |
|-----------|-------------|-----------------|-----------------|
| 0.24 deg | 0.36 deg | 1% | 1.2% |

kHz over a period of 2 s. The postprocessing is done for three consecutive rotor pitches. The sampling rate resolves 82 points in the relative frame of reference. Table 1 gives the typical measurement uncertainties of the FRAP probe.

2.3 Measurement Plane. The spatial resolution of the measurement grid consisted of 39 radial and 40 circumferential points (covering one stator pitch) with a radial clustering near the endwalls. The data are acquired at a sampling rate of 200 kHz over a period of 2 s. The postprocessing is done for three consecutive rotor pitches. The temporal resolution is 82 points per blade passing period.

3 Results and Discussion

In Sec. 3.2 and 3.3, the time-resolved flowfield data are presented. The analysis focuses on the changes of the secondary flow features. The data case has axisymmetric endwalls, while the profiled case has nonaxisymmetric hub and tip endwalls in stator 1 and a nonaxisymmetric rotor hub endwall.

3.1 Operating Conditions. During the measurements, the turbine 1.5 stage total-to-static pressure ratio is kept constant at $\Pi_{1,5}=1.65$. The constant entry temperature is kept constant to permit an accurate comparison between measurements made on different days. To account for the change in ambient pressure on different measurement days, the pressures are nondimensionalized by the respective inlet total pressure. Table 2 gives the operating conditions as well as the characteristic geometrical parameters.

Figure 2 shows the geometry and the relative positions of stators 1 and 2, as well as the relative position of the traverse planes S1ex and R1ex.

3.2 First Stator Exit Flow Field. Figure 3 shows the total pressure field at the exit of stator 1. The plots show a downstream view of one stator pitch at the same relative blade position. Although it is generally considered sufficient to look at steady data to evaluate the flow field of a stationary row, the current result illustrates that there is already a strong unsteady signature at the exit of stator 1 due to the downstream rotor. This unsteady signature results from the unsteady work done by the rotor upstream potential field, also termed as the bow wave.

One can identify clearly the stator secondary flows and the wake as low total pressure regions. The core of the hub passage vortex (HPV) extends from about 5–15% span, while the tip passage vortex core lies between 80% and 90% spans. The high total pressure zone to the left of the pitch centerline is the signature of

Table 2 Operating conditions and characteristics of geometry

| | | |
|--|------------------|----------------------------|
| $\Pi_{1,5}$ | $1.65 \pm 0.4\%$ | |
| $T_{t,in}$ | 328 ± 0.2 | K |
| $\frac{\dot{m}\sqrt{T_{t,in}}}{N}$ | $152 \pm 0.2\%$ | kg K ^{1/2} /s bar |
| $\frac{p_{t,in}}{N\sqrt{T_{t,in}}}$ | 2.48 ± 0.05 | rps/K ^{1/2} |
| Aspect ratio (S1/R1/S2) | 0.87/1.17/0.82 | |
| Mach number (S1/R1/S2) | 0.54/0.26/0.46 | |
| Reynolds number (S1/R1/S2) ($\times 10^5$) | 7.1/3.8/5.1 | |
| Blade count (S1/R1/S2) | 36/54/36 | |

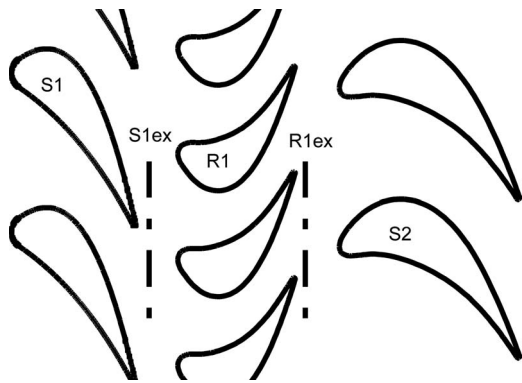


Fig. 2 Illustration of geometrical relations

the rotor bow wave. The low total pressure cores at hub and tip, as well as in the wake region, are more pronounced in the axisymmetric case.

Figure 4 shows the pitch angle variation in the time-space format at midheight, which is shown as line Y in Fig. 3. Inside the wake, there is a much stronger inward pitch angle in the axisymmetric case identified as the white region, as well as a strong outward pitch angle shown as the dark color regions. This results in a stronger circumferential pitch angle gradient than for the profiled case. This stronger gradient is the signature of stronger trailing edge vorticity due to the variation in lift up the span. Therefore, there is more streamwise vorticity, as well as higher dissipation within the wake. As a result there is more loss at midheight in the datum case.

In order to better understand the unsteady rotor-stator interaction, time-space diagrams at three radial heights corresponding to the lines X , Y , and Z in Fig. 3 are presented in Fig. 5. The first cut at $Z=10\%$ span goes through the hub passage vortex, the second cut at midheight Y shows the wake interaction, and the third cut at $X=82\%$ details the tip passage vortex. Vertically oriented features in the stationary frame space-time diagrams can be attributed to the stator flowfield, while rotor flow features show up as inclined parallel structures. The inclined highest total pressure regions in Fig. 5 are the rotor bow waves. The low total pressure region at 0.3 pitch is either the stator secondary flow or the wake depending on the radial height. When this region interacts with the rotor leading edge, its total pressure increases close to the freestream level. One can also see the wake that moves circumferentially as it interacts with the rotor leading edge. At the hub of the baseline

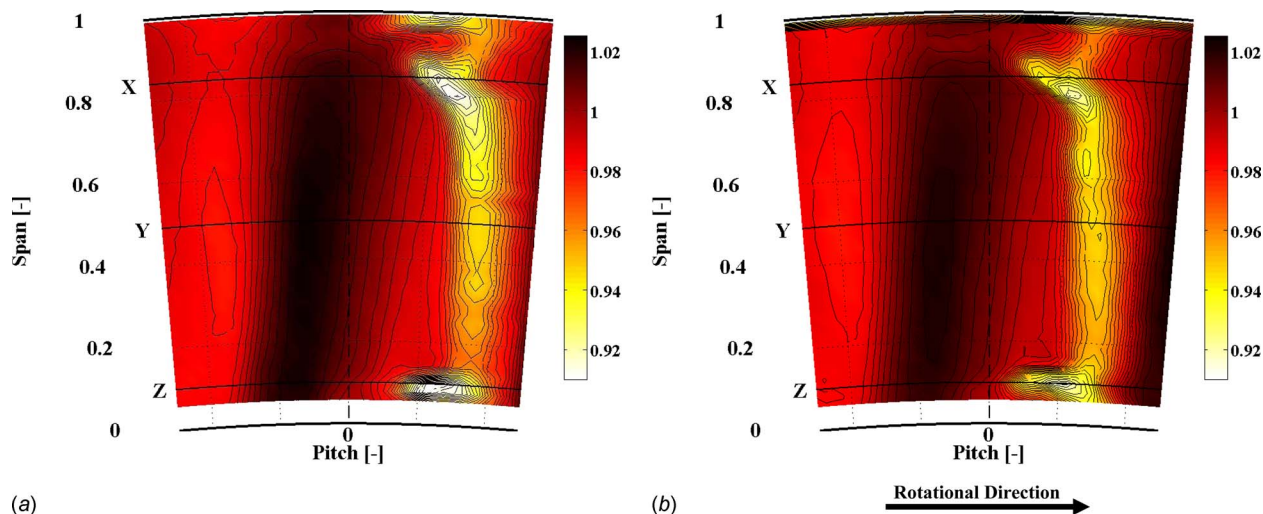


Fig. 3 Total pressure at traverse plane S1ex

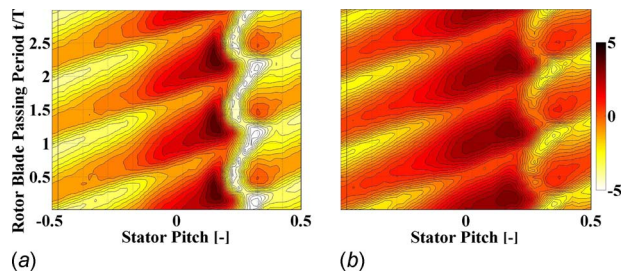


Fig. 4 Time-space diagram: pitch angle at traverse plane S1ex

case, the rotor-stator interaction is stronger. The endwall profiling shows beneficial changes at all three heights. The low total pressure regions are smaller and less profound in the profiled case. However, the effect at midheight is strongest because of the reduced shed vorticity in the profiled case. This effect was not anticipated in the design phase.

Figure 5 shows that endwall profiling in low aspect ratio turbines reduces the losses both in the endwall region and also at midheight. At height Z the profiled case seems to be more homogeneous in the freestream region compared with the baseline measurement.

Figure 6 shows the relative total pressure at midheight. The circumferential coordinate given as a fractional of stator pitch is plotted against time. One can see an underlying variation in the stator pitch direction due to the potential field of the vane. This creates work lines in the relative frame. It can be seen as much larger regions of low relative total pressure in the data case. In the freestream the relative total pressure varies over time. This is the result of a time variation of the rotor lift and indicates unsteady flow in the rotor frame of reference.

3.3 Rotor Exit Flow Field. Time resolved. The unsteady interaction of stator 1 flow features and the rotor flow features are next examined. A good indicator of flow features are the root mean square (rms) values of the random part of the total pressure signal. Regions of high rms are indicative of eddy shedding or regions of high turbulence. Using the triple decomposition of the time-resolved pressure signal, as shown in Eq. (1), the random part $p'(t)$ can be evaluated as the difference between the raw pressure $p(t)$ signal of the FRAP probe and the phase-locked averaged pressure $\bar{p} + \tilde{p}(t)$. The same approach was used by Porreca et al. [23] to derive turbulent quantities.

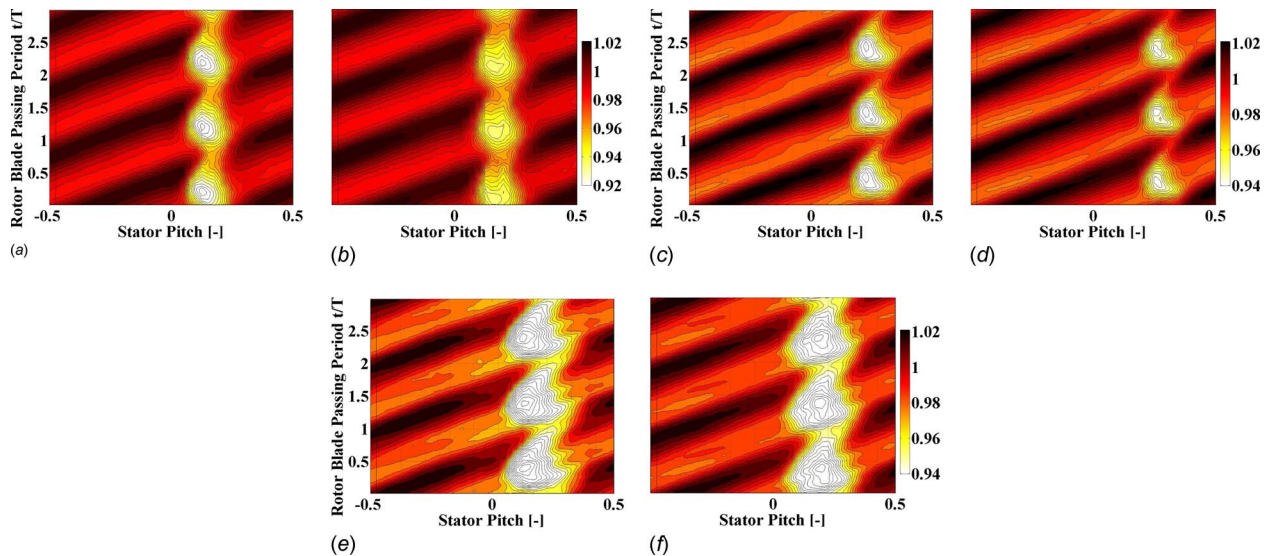


Fig. 5 Time-space diagram: total pressure at traverse plane S1ex

$$p(t) = \bar{p} + \bar{p}'(t) + p'(t) \quad (1)$$

Figure 7 shows the downstream view of the relative total pressure field of two stator pitches at one instant in time. One can see the secondary flow features of the three blades as three low relative total pressure zones. From 90% span to the tip, one can identify the loss core of the tip leakage vortex labeled as 1 in between 60% and 80% spans the loss core of the rotor tip passage vortex 2 and finally between 15% and 35% spans the loss core of the rotor

hub passage vortex 3.

The two passage vortices are connected by the rotor wake. The shape of the loss cores of the secondary flow features changes between different zones of interaction (A–C).

Figures 8 and 9 show the normalized relative total pressure and rms in space-time diagrams. The diagonal bands of low relative total pressure and high rms are associated with the rotor wake. One sees only minor differences between the data and profiled cases. At 0% pitch the upstream potential effect of the second stator is seen as a high relative total pressure zone. Furthermore, there is a horizontal feature of high relative total pressure and high rms labeled 1. This zone shows the remains of the stator 1 wake. The data case shows a much larger zone of high relative total pressure, which also contains higher unsteadiness in terms of rms. The wake of stator 1 shows a 4% increase of relative total pressure of the stage total pressure drop over the rotor in both cases. This indicates that work is done on the wake in the relative frame, which is consistent with the results presented in Ref. [24].

The more extended high relative total pressure zone in the data case results in greater mixing loss and lower efficiency. Based on the stationary flow field, one can differentiate between the three interaction zones. The traverses, marked as A–C in Figs. 7–9 are

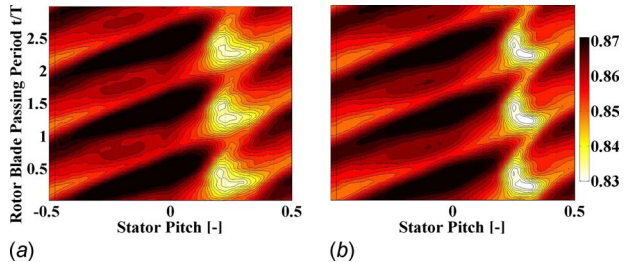


Fig. 6 Time-space diagram: relative total pressure at traverse plane S1ex

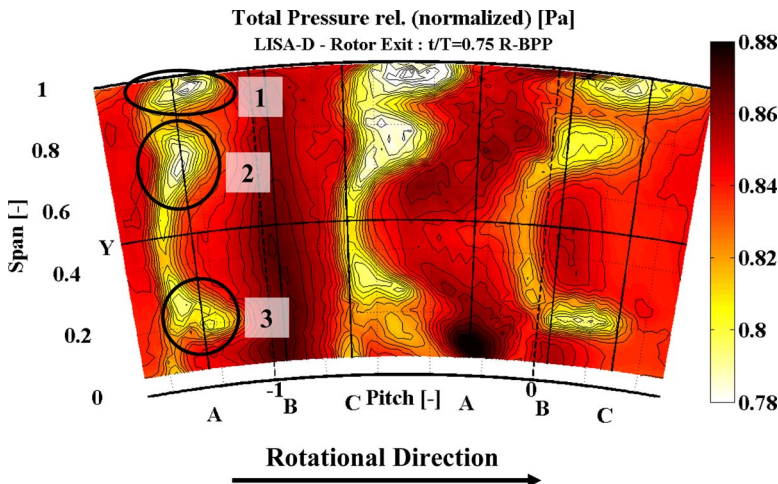


Fig. 7 Relative total pressure at traverse plane R1ex

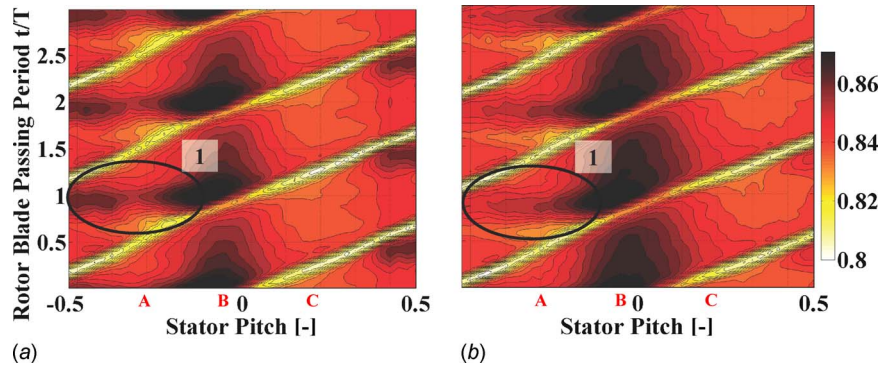


Fig. 8 Time-space diagram: relative total pressure at traverse plane R1ex

representatives of these three interaction zones. In zone A, the rotor flow features interact with flow features coming from the upstream vane characterized by a region of high rms between the two rotor wakes. Traverse B shows the interaction of the rotor secondary flows with the leading edge of the downstream stator, seen as a high relative total pressure zone in Fig. 8. Finally, along traverse C there are no significant rotor-stator interactions characterized by low rms values in the freestream region between the two rotor wakes.

In order to further analyze the interactions, the three radial

traverses at A–C are plotted against time, seen in Figs. 10 and 11. Figure 10 shows the radial-time diagram of the root mean square values of the random part of the total pressure signal. One can differentiate between different levels of unsteadiness in the three cases. The regions of high rms are indicative of a potential source of loss that subsequently dissipates and causes a rise in entropy.

Figures 10(e) and 10(f) representing traverse C show only minimal rotor-stator interactions characterized by the lowest integral rms values. The rotor flow features identified in Fig. 7 can be seen as high rms regions. From 90% span to the tip, one can identify

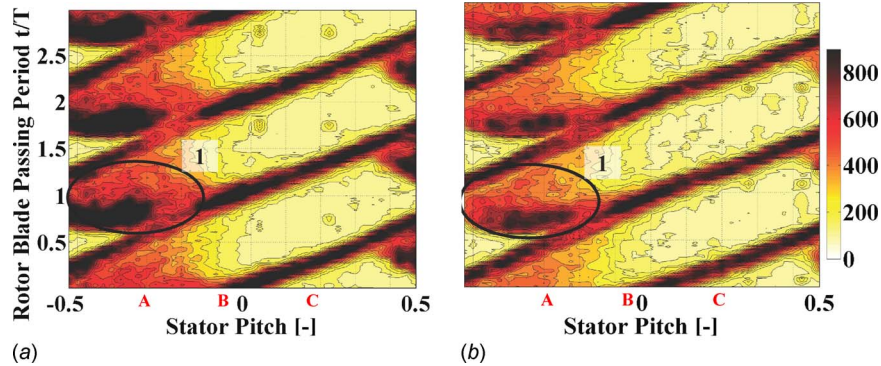


Fig. 9 Time-space diagram: rms of the total pressure random part at traverse plane R1ex (Pa)

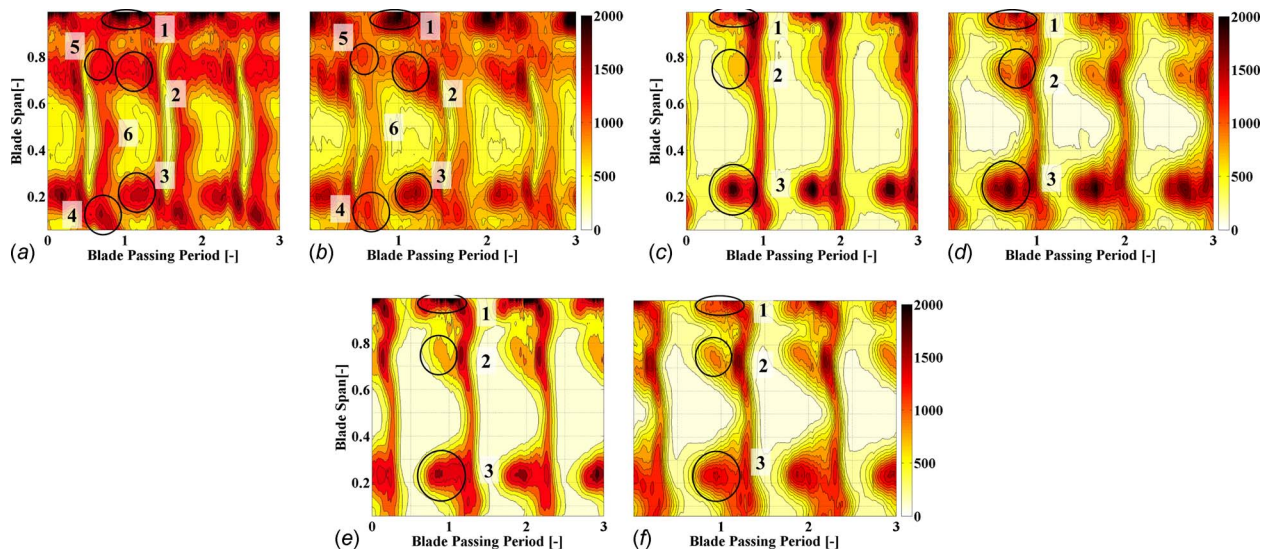


Fig. 10 rms of the total pressure random part at traverse plane R1ex (Pa)

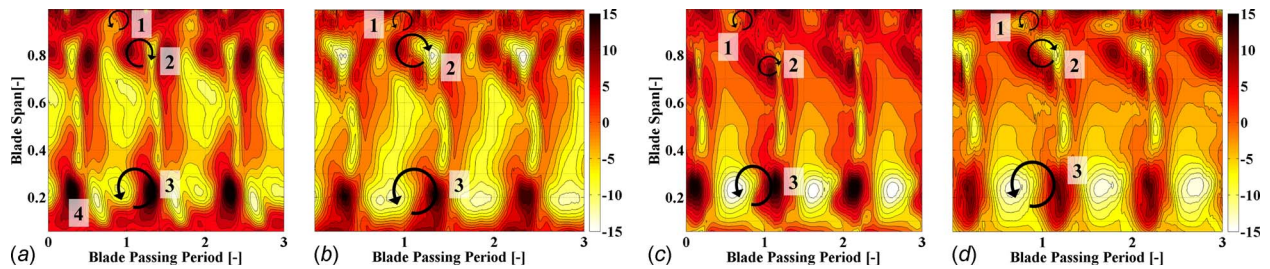


Fig. 11 Pitch angle at traverse plane R1ex

the tip leakage vortex labeled with 1 in between 60% and 80% spans the rotor tip passage vortex 2 and finally between 15% and 35% spans the rotor hub passage vortex 3. With endwall profiling, the unsteadiness of the hub passage was reduced. The tip passage vortex is almost unaltered, while the tip leakage vortex was reduced with endwall profiling.

In traverse B, the unsteadiness in the rotor hub passage vortex rises due to the interaction with the downstream stator leading edge. In the profiled case, the rotor hub passage vortex seems to be larger but less intense in terms of the unsteadiness.

Along traverse A the integral rms values rise once more as additional high rms zones occur. These zones show the remains of the upstream vane flow features. There is a high rms zone at the hub labeled 4 associated with the upstream vane hub passage vortex. With endwall profiling this region has reduced in size and intensity. The high rms zone at 70% span labeled 5 can be associated with the vane tip passage vortex. Also, this zone has reduced in size and intensity in the profiled case. Finally, there is the high rms zone labeled 6, which can be identified as the residual signature of the upstream stator wake. Also the rms values in this region have reduced with endwall profiling. In traverse A, the unsteadiness has decreased profoundly with endwall profiling. This is mainly a consequence of improvements in stator 1.

Figure 11 shows the radial-time diagram for the pitch angle of the radial traverses A and C. If streamwise vorticity is present in a flowfield, one will find circumferential gradients of pitch angle. As the rotor vortices travel circumferentially through the radial traverse, time gradients seen in Fig. 11 are related to circumferential pitch angle gradients in the rotor frame of reference.

Figures 11(c) and 11(d) show the pitch angle distribution of traverse C. Between 15% and 35% spans, there is a positive time-wise pitch angle gradient associated with the rotor hub passage 3. With endwall profiling, this gradient has reduced by $\Delta\gamma = 10.2$ deg per blade passing period from $\gamma = 65$ deg per blade passing period in the baseline case. At around 80% span, there is a pitch angle gradient of opposite sign, which is induced by the tip passage vortex 2. The region of negative pitch in the profiled case is much more pronounced. The minimum pitch at 80% is 6 deg lower in the profiled case. Around 90% span, there is another

pitch angle gradient, which is associated with the tip leakage vortex 1. The gradient is modest in both cases leading to the conclusion that the tip leakage flow is only of modest vortical nature.

Figures 11(a) and 11(b) shows the radial-time diagram of traverse A. In the data case, there is a strong negative pitch angle zone labeled 4 that is coincident with the high rms zone associated with the vane hub passage vortex. In the profiled case, this zone has merged with the low pitch angle region of the rotor hub passage vortex leading to a reduction in pitch angle gradients near the hub.

Figure 12 shows the radial-time diagram of the total pressure for traverse A. The rotor loss features are seen as low total pressure zones. However, the hub loss features that originate from the upstream vane, which are seen as regions of high rms in Fig. 10 and of low pitch angle in Fig. 11, have a higher total pressure level compared with the freestream region 4. In the profiled case, the region labeled 4 is more homogenous. The inhomogeneities in the data case will mix out and result in higher losses.

Using the rms plots, the vane and rotor loss cores at the exit of the rotor can be identified and the associated rotor exit total pressure values of the stator 1 wake and hub passage vortex can be also determined. The freestream total pressure value at rotor exit is defined as the total pressure value coincident with the lowest rms region in traverse A. The rotor inlet freestream total pressure is defined as the time-averaged midspan value at -0.2 pitch. The stator 1 wake total pressure value at rotor inlet is defined as the minimum value at midspan. The upstream vane hub passage vortex total pressure at rotor inlet is defined as the minimum value at height Z . Using these values, the total pressure drop of the stator 1 wake and hub passage vortex fluid, as well as the total pressure drop in the freestream, can be calculated. Table 3 gives the total pressure drop of the freestream and the upstream vane wake and hub passage vortex. The pressure drop is nondimensionalized by the average stage total pressure drop. There is a 20% less total pressure drop of the stator 1 loss regions compared with the freestream. The loss features of the profiled case show 3.8% and 2.5% higher total pressure drops in the wake and hub passage vortex, respectively. This means that there is a higher work extraction in the profiled case, which contributes to the higher effi-

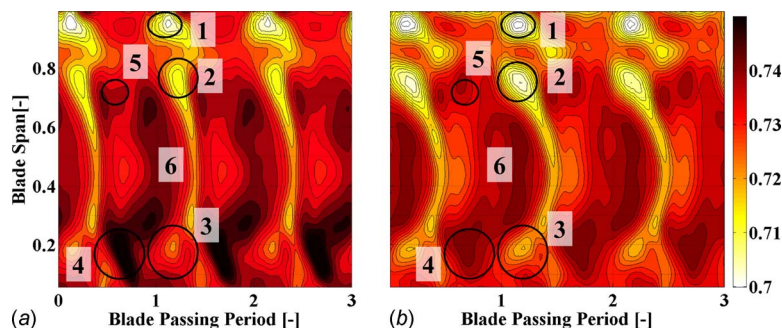


Fig. 12 Total pressure at traverse plane R1ex

Table 3 Nondimensional total pressure drop

| | Data | Profiled | $\Delta\%$ |
|------------|------|----------|------------|
| Freestream | 1.0 | 1.0 | |
| S1 Wake | 0.78 | 0.81 | 3.8% |
| S1 HPV | 0.80 | 0.82 | 2.5% |

ciency. These results show that the upstream nozzle guide vane wake and vortices do less work on the rotor than the freestream, a conclusion that is consistent with the ideas presented in Ref. [24].

3.4 Streamwise Vorticity. The time-averaged streamwise vorticity and the dissipation function are next examined. The streamwise vorticity is the scalar product of the vorticity, whose components are given in Eqs. (2)–(4) and the primary flow vector. The streamwise vorticity is related to secondary flows as it introduces flow perpendicular to the primary flow direction, defined as the circumferentially mass-averaged velocity profile. Therefore, a reduction in streamwise vorticity normally leads to a reduction in secondary loss. To calculate the three-dimensional vorticity vector, the axial gradients of the radial and circumferential velocity components are needed. In a single axial plane traverse, it is not possible to calculate these axial gradients.

$$\Omega_x = \frac{1}{r} \left(\frac{\partial}{\partial r} (ru_\theta) - \frac{\partial u_r}{\partial \theta} \right) \quad (2)$$

$$\Omega_r = \frac{1}{r} \frac{\partial u_x}{\partial \theta} - \frac{\partial u_\theta}{\partial x} \quad (3)$$

$$\Omega_\theta = \frac{\partial u_r}{\partial x} - \frac{\partial u_x}{\partial r} \quad (4)$$

Therefore, the axial gradients are estimated using the time-resolved data, with the assumption that the flow structures are frozen over one timestep. Multiplane measurements performed subsequent to this paper verify that this assumption is valid; these measurements will be presented in a future publication. For example, the following approximation for the axial derivative of the radial velocity can be used:

$$\frac{\partial u_r}{\partial x} \approx \frac{\partial u_r}{u_x \cdot \partial t} \quad (5)$$

This approach is only correct if the flow direction is within a very small range such as ± 10 deg, with respect to the axial direction. For a larger range, it is necessary to interpolate in the circumferential direction using the circumferential displacement $d\theta$ of a fluid particle over one timestep t . So if the fluid particle is traveling in positive circumferential direction, it is displaced by $-d\theta$ relative to the traverse Tr in the preceding timestep. Therefore, an interpolation within the measurement grid consisting of the radial traverses Tr is required to determine the velocity at the same circumferential position. Equation (5) is then rewritten as Eq. (6) and illustrated in Fig. 13.

$$\frac{\partial u_r}{\partial x} \approx \frac{u_r(t, \theta) - u_r(t+1, \theta + d\theta)}{u_x \cdot dt} \quad (6)$$

Figure 14 shows the streamwise vorticity at stator exit time averaged in the stationary frame of reference. At 85% span, there is a region of positive streamwise vorticity 3, which is associated with the tip passage vortex. Zone 1 shows the vorticity of the opposite sign that represents the tip trailing shed vortex. Zone 2 shows the negative streamwise vorticity of the hub passage vortex. Zone 4 shows the positive vorticity that represents the hub trailing shed vortex. Between 15% and 75% spans, there is a band of positive vorticity that is associated with trailing shed vorticity 5. This trailing shed vorticity has been reduced by a factor of 2

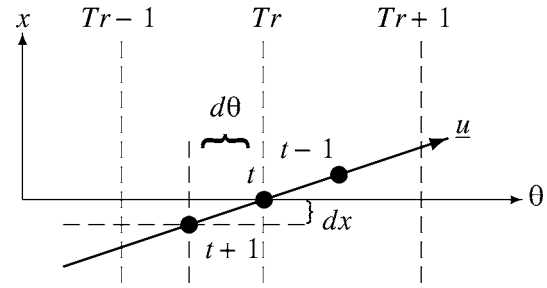


Fig. 13 Illustration for circumferential interpolation

with nonaxisymmetric endwall contouring.

Figure 15 shows the streamwise vorticity at rotor exit time averaged in the rotating frame of reference. The positive streamwise vorticity at 20% span is due to the rotor hub passage vortex labeled 3. It is therefore evident that the nonaxisymmetric rotor hub endwall reduces the vorticity of the hub passage vortex as was the design intent. Zone 5 shows the negative streamwise vorticity of the hub trailing edge shed vortex. It is therefore evident that the nonaxisymmetric rotor hub endwall also reduces the strength of the hub trailing shed vortex. At 75% there is a region of negative streamwise vorticity 2. This region is associated with the tip passage vortex. Zone 4 shows the tip trailing shed vortex. Along the casing the positive vorticity signature of the tip leakage vortex is seen in zone 1. As the turbine has an unshrouded rotor, no endwall contouring at the tip is possible. The tip gap size is only changed by 1% of gap size. Therefore, the observed changes in the outer part of the annulus come from the different stator 1 exit flow field. One sees an increase in vorticity in the tip passage vortex region as well as a reduction in the tip leakage region with endwall profiling.

3.5 Dissipation. The rate of irreversible heat generation by doing work against the viscous forces is given in Eq. (7) given in Ref. [25]. The viscosity in Eq. (7) is the molecular or laminar viscosity. In order to evaluate the dissipation correctly, one would need a fine spatial resolution. The instantaneous velocity vector with its deterministic and turbulent fluctuations is also needed. In practice, the spatial resolution is limited by the traverse grid size and the temporal resolution is only deterministic. For these reasons, the calculated dissipation must be regarded with some care as the modest spatial resolution and the deterministic time signature will result in an underestimate of the dissipation.

$$dQ_F = dt \cdot \Delta V \cdot \mu \cdot \Phi \quad (7)$$

Φ , the viscous dissipation function, is given in cylindrical coordinates in Eq. (8). The required axial gradients are approximated in the same manner as for the streamwise vorticity shown in Fig. 13 and given in Eq. (6).

$$\begin{aligned} \Phi = 2 & \left[\left(\frac{\partial u_r}{\partial r} \right)^2 + \left(\frac{1}{r} \frac{\partial u_\theta}{\partial \theta} + \frac{u_r}{r} \right)^2 + \left(\frac{\partial u_x}{\partial x} \right)^2 \right] \\ & + \left[r \frac{\partial}{\partial r} \left(\frac{u_\theta}{r} \right) + \frac{1}{r} \frac{\partial u_r}{\partial \theta} \right]^2 + \left[\frac{1}{r} \frac{\partial u_x}{\partial \theta} + \frac{\partial u_\theta}{\partial x} \right]^2 \\ & + \left[\frac{\partial u_r}{\partial x} + \frac{\partial u_x}{\partial r} \right]^2 - \frac{2}{3} (\nabla \cdot \mathbf{u})^2 \end{aligned} \quad (8)$$

In order to better quantify the dissipation function, it is normalized by the flux of kinetic energy given in

$$\dot{m} \cdot \frac{u^2}{2} = \rho \cdot u_x \cdot A_x \cdot \frac{u^2}{2} \quad (9)$$

where

$$u^2 = u_x^2 + u_r^2 + u_\theta^2 \quad (10)$$

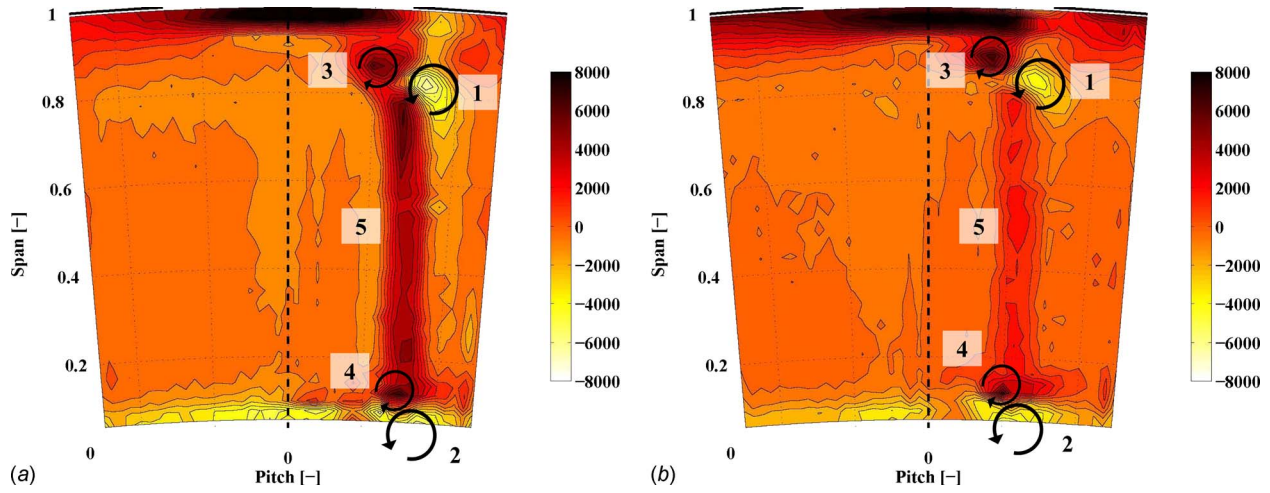


Fig. 14 Time-averaged streamwise vorticity in the stator frame of reference at traverse plane S1ex (1/s)

Thus we have the modified dissipation function D given in

$$D = \frac{\mu \cdot \Phi}{\rho \cdot \frac{u^2}{2}} \quad (11)$$

Figure 16 shows the time-averaged dissipation function at the stator exit in the stationary frame of reference. For purposes of scaling, we present contours of the D parameter. D can be interpreted as the percentage rate at which kinetic energy is converted into heat per second. It should be noted that Fig. 16 shows the

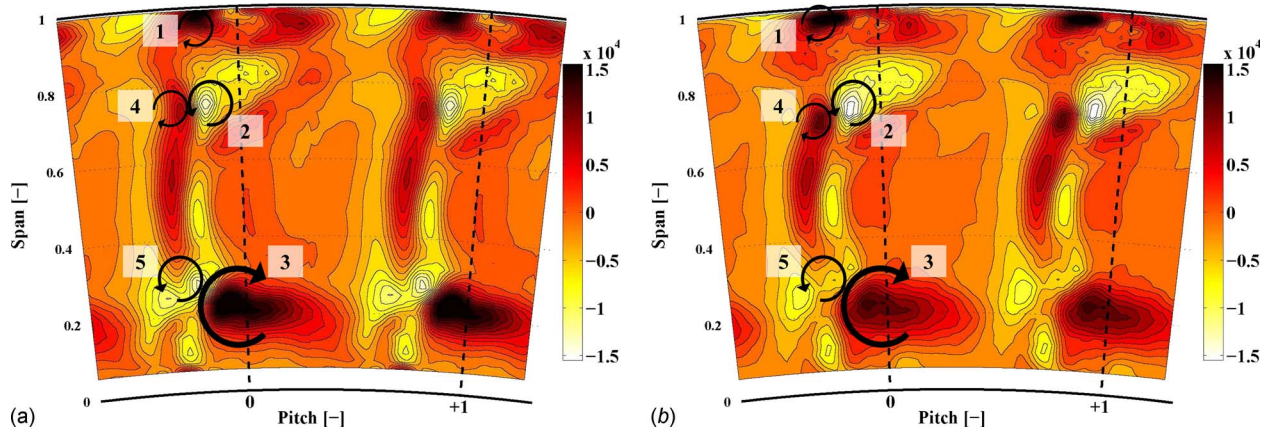


Fig. 15 Time-averaged streamwise vorticity in the rotor frame of reference at traverse plane R1ex (1/s)

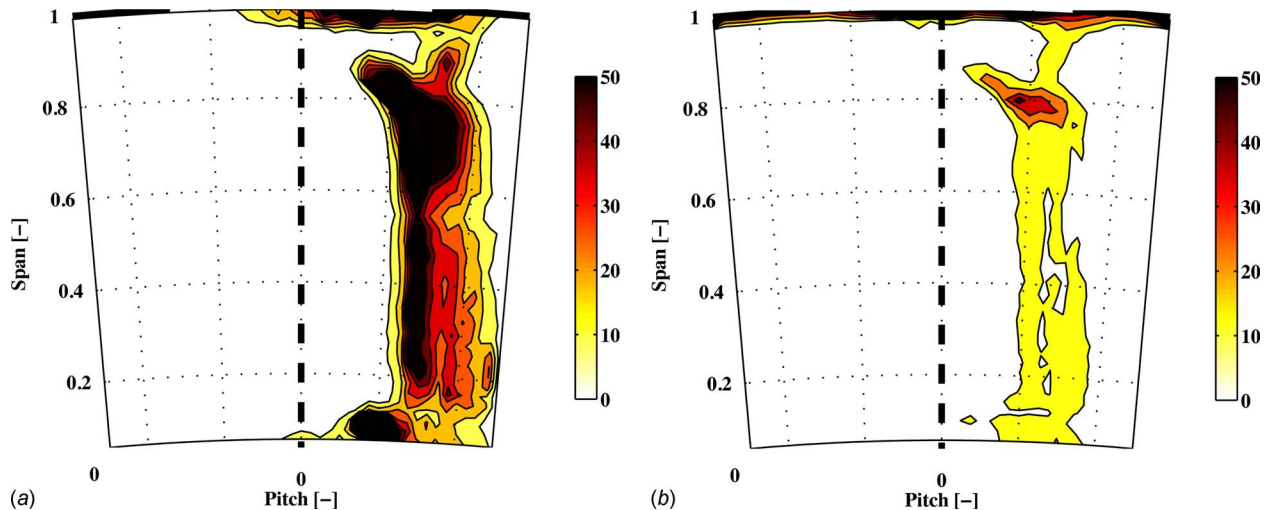


Fig. 16 Time-averaged D parameter in the stator frame of reference at traverse plane S1ex (%/s)

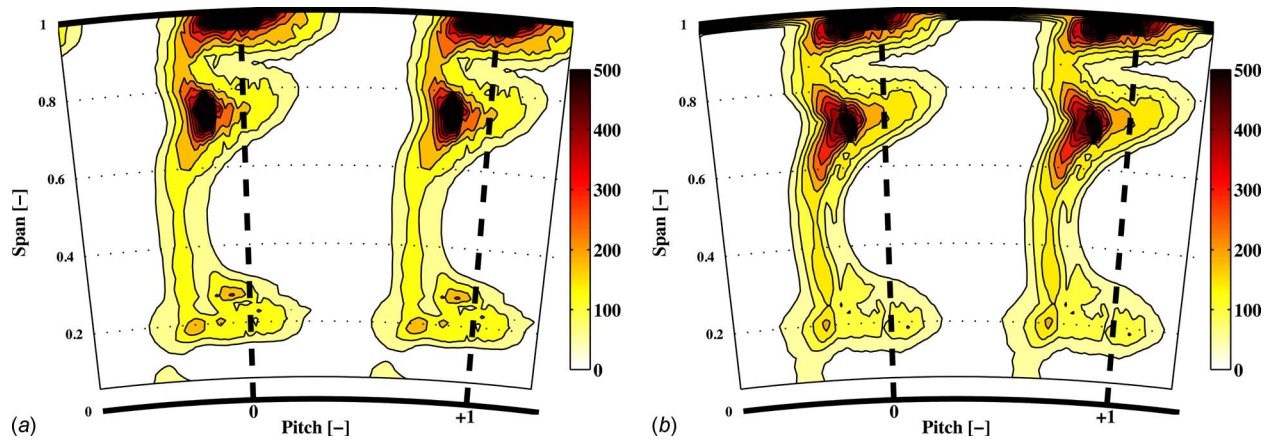


Fig. 17 Time-averaged D parameter in the rotor frame of reference at traverse plane R1ex (%/s)

dissipation over only one single traverse plane. In order to relate the dissipation to loss, one would need to integrate over the whole volume. Nevertheless the nonaxisymmetric profiling considerably reduces the D parameter over the whole span. This is a good indication of the observed loss reduction. At the casing the high dissipation region in the nonaxisymmetric case is confined to the endwall, whereas it is accumulated in the baseline case. The dissipation in the wake of the axisymmetric case is four to five times higher. At the hub the zone of high dissipation is no longer visible in the nonaxisymmetric case.

Figure 17 shows the time-averaged D parameter at rotor exit in the rotating frame of reference. In Fig. 17 the dissipation is much stronger than at the exit of the upstream nozzle guide vane, as shown in Fig. 16. The scale is an order of magnitude greater. The highest values are measured both in the tip leakage region and in the interaction zone of the trailing edge shed vortex and the tip passage vortex. The dissipation at the hub is much less pronounced and reduced with endwall profiling. At 75% span, the integrated dissipation is about the same. However, the axisymmetric case shows a more intense core, while the core is diffused over a larger area in the nonaxisymmetric case.

4 Conclusions

The results shown in this paper provide detailed explanations for the improved efficiency of about $\Delta\eta_{tt}=1.0\%$. In this particular design, most of the improvement can be found in the first vane row. With a new approach using time derivatives, the streamwise vorticity could be calculated from a single plane traverse. Doing this it became evident that the endwall profiling has suppressed the streamwise vorticity of the secondary flow in stator 1 and the rotor hub as intended in the design. However, it was found that the main reductions in streamwise vorticity with profiling, more than 50%, were achieved in the nozzle wake due to the reduced trailing shed vorticity. The dissipation function in the wake at nozzle guide vane exit is reduced by a factor of 5 with nonaxisymmetric endwall profiling. The reduction in streamwise vorticity and dissipation are mainly responsible for the stator 1 loss reduction of 12% reported in the first part of this two part paper.

The rotor hub endwall profile contributed to the total efficiency increase by reducing the streamwise vorticity of the hub passage vortex. The less distorted stator flowfield of the profiled case, which enters the rotor leads potentially to a larger work extraction, as well as to a more homogenous rotor exit field. With a more homogenous rotor exit flowfield, the mixing losses are reduced. At rotor exit it was possible to identify the wake and loss cores of the upstream vane via their rms signature. The variation in pitch angle and relative total pressure in the zone of rotor and upstream vane interaction seem to have reduced with endwall profiling.

Acknowledgement

The work reported here was carried out within the joint industrial and academic research program that is part of the “Luftfahrtforschungsprogramm LuFo3” supported by the German Federal Ministry of Economics and Technology.

Nomenclature

| | |
|-------------|--|
| A | = area (m^2) |
| D | = dissipation function (%/s) |
| h | = enthalpy (J/kg) |
| \dot{m} | = massflow (kg/s) |
| N | = rotational speed (rps) |
| p | = pressure (Pa) |
| \bar{p} | = time mean part of pressure signal (Pa) |
| \tilde{p} | = periodic part of pressure signal (Pa) |
| p' | = random part of pressure signal (Pa) |
| Q | = amount of heat (J) |
| r | = radial coordinate (m) |
| T | = temperature (K) |
| T | = blade period (s) |
| t | = time (s) |
| U | = mean height blade speed (m/s) |
| u | = velocity (m/s) |
| V | = volume (m^3) |
| x | = axial coordinate (m) |

Greek

| | |
|----------|------------------------------------|
| η | = efficiency |
| θ | = circumferential coordinate (m) |
| μ | = viscosity (kg/ms) |
| Π | = pressure ratio |
| ρ | = density (kg/m^3) |
| Φ | = dissipation function ($1/s^2$) |
| Ω | = vorticity ($1/s$) |

Subscripts

| | |
|-----------|------------------------------|
| c, \max | = compressor |
| F | = frictional |
| in | = turbine inlet |
| r | = radial coordinate |
| t | = stagnation flow quantity |
| tt | = total-to-total |
| x | = axial coordinate |
| θ | = circumferential coordinate |
| 1.5 | = total-to-static 1.5 stages |

Abbreviations

| | |
|------|-----------------------------------|
| FRAP | = fast response aerodynamic probe |
|------|-----------------------------------|

HPV = hub passage vortex
 NGV1 = first nozzle guide vane
 NGV2 = second nozzle guide vane
 rms = root mean square
 R1ex = rotor 1 exit
 R1 = rotor 1
 R1ex = rotor 1 exit
 S1ex = stator 1 exit
 S1 = stator 1
 S2 = stator 2
 Tr = traverse number

References

- [1] Dunham, J., 1970, "A Review of Cascade Data on Secondary Losses in Turbines," *J. Mech. Eng. Sci.*, **12**(1), pp. 48–59.
- [2] Sieverding, C. H., 1985, "Recent Progress in the Understanding of Basic Aspects of Secondary Flows in Turbine Blade Passages," *Trans. ASME: J. Eng. Gas Turbines Power*, **107**(2), pp. 248–257.
- [3] Langston, L. S., Nice, M. L., and Hooper, R. M., 1977, "3-Dimensional Flow Within a Turbine Cascade Passage," *ASME J. Eng. Power*, **99**(1), pp. 21–28.
- [4] Schlienger, J., Kalfas, A. I., and Abhari, R. S., 2005, "Vortex-Wake-Blade Interaction in a Shrouded Axial Turbine," *ASME J. Turbomach.*, **127**(4), pp. 699–707.
- [5] Sturm, W., Scheugenpflug, H., and Fottner, L., 1992, "Performance Improvements of Compressor Cascades by Controlling the Profile and Sidewall Boundary-Layers," *ASME J. Turbomach.*, **114**(3), pp. 477–486.
- [6] Biesinger, Th. E., 1993, "Secondary Flow Reduction Techniques in Linear Turbine Cascades," Ph.D. thesis, University of Durham, Durham, UK.
- [7] Harrison, S., 1992, "The Influence of Blade Lean on Turbine Losses," *ASME J. Turbomach.*, **114**(1), pp. 184–190.
- [8] Dejc, M. E., and Zarjankin, A. E., 1960, "Methods of Increasing the Efficiency of Turbine Stages," *Teploenergetika (Moscow, Russ. Fed.)*, **2**, pp. 18–24.
- [9] Morris, A. W. H., and Hoare, R. G., 1975, "Secondary Loss Measurements in a Cascade of Turbine Blades With Meridional Wall Profiling," *ASME Paper No. 75-WA/GT-13*.
- [10] Atkins, M. J., 1987, "Secondary Losses and End-Wall Profiling in a Turbine Cascade," *Proceedings of IMechE Turbo Conference*, C255(87), pp. 29–42.
- [11] Sauer, H., Muller, R., and Vogeler, K., 2001, "Reduction of Secondary Flow Losses in Turbine Cascades by Leading Edge Modifications at the Endwall," *ASME J. Turbomach.*, **123**(2), pp. 207–213.
- [12] Rose, M. G., 1994, "Non-Axisymmetric Endwall Profiling in the HP NGVs of an Axial Flow Gas Turbine," *ASME Paper No. 94-GT-249*.
- [13] Hartland, J. C., Gregory-Smith, D. G., Harvey, N. W., and Rose, M. G., 2000, "Nonaxisymmetric Turbine End Wall Design: Part II—Experimental Validation," *ASME J. Turbomach.*, **122**(2), pp. 286–293.
- [14] Ingram, G. L., Gregory-Smith, D. G., Rose, M. G., Harvey, N. W., and Brennan, G., 2002, "The Effect of End-Wall Profiling on Secondary Flow and Loss Development in a Turbine Cascade," *ASME Paper No. GT-2002-30339*.
- [15] Brennan, G., Harvey, N. W., Rose, M. G., Fomison, N., and Taylor, M. D., 2001, "Improving the Efficiency of the Trent 500 HP Turbine Using Non-Axisymmetric End Walls: Part I: Turbine Design," *ASME Paper No. 2001-GT-0444*.
- [16] Rose, M. G., Harvey, N. W., Seaman, P., Newman, D. A., and McManus, D., 2001, "Improving the Efficiency of the Trent 500 HP Turbine Using Non-Axisymmetric End Walls: Part II: Experimental Validation," *ASME Paper No. 2001-GT-0505*.
- [17] Duden, A., Raab, I., and Fottner, L., 1998, "Controlling the Secondary Flow in a Turbine Cascade by 3D Airfoil Design and Endwall Contouring," *ASME Paper No. 98-GT-072*.
- [18] Eymann, S., Foerster, W., Beversdorf, M., Reinmoeller, U., Niehuis, R., and Gier, J., 2002, "Improving 3D Flow Characteristics in a Multistage LP Turbine by Means of Endwall Contouring and Airfoil Design Modification: Part I: Design and Experimental Investigation," *ASME Paper No. GT-2002-30352*.
- [19] Sell, M., Schlienger, J., Pfau, A., Treiber, M., and Abhari, R. S., 2001, "The 2-Stage Axial Turbine Test Facility LISA," *ASME Paper No. 2001-GT-0492*.
- [20] Behr, T., Kalfas, A. I., and Abhari, R. S., 2007, "Unsteady Flow Physics and Performance of a One-and-1/2-Stage Unshrouded High Work Turbine," *ASME J. Turbomach.*, **129**(2), pp. 348–359.
- [21] Kupferschmied, P., Kopperl, O., Gizzi, W. P., and Gyarmathy, G., 2000, "Time Resolved Flow Measurements With Fast Aerodynamic Probes in Turbomachinery," *Meas. Sci. Technol.*, **11**, pp. 1036–1054.
- [22] Pfau, A., Schlienger, J., Kalfas, A. I., and Abhari, R. S., 2003, "Unsteady 3-Dimensional Flow Measurement Using a Miniature Virtual 4 Sensor Fast Response Aerodynamic Probe (FRAP)," *ASME Paper No. GT2003-38128*.
- [23] Schlichting, H., 1951, *Grenzschicht-Theorie*, G. Braun, Karlsruhe, Germany.
- [24] Porreca, L., Hollenstein, M., Kalfas, A. I., and Abhari, R. S., 2007, "Turbulence Measurements and Analysis in a Multistage Axial Turbine," *J. Propul. Power*, **23**(1), pp. 227–234.
- [25] Rose, M. G., and Harvey, N. W., 2000, "Turbomachinery Wakes: Differential Work and Mixing Losses," *ASME J. Turbomach.*, **122**(1), pp. 68–77.